HHS Public Access

Author manuscript

Nat Mater. Author manuscript; available in PMC 2019 June 26.

Published in final edited form as:

Nat Mater. 2016 March ; 15(3): 353–363. doi:10.1038/nmat4497.

Self-assembled RNA-triple-helix hydrogel scaffold for microRNA modulation in the tumour microenvironment

João Conde[1,2,*], **Nuria Oliva**[1], **Mariana Atilano**[1,3], **Hyun Seok Song**[1,4], and **Natalie Artzi**[1,5,6,*]

[1]Massachusetts Institute of Technology, Institute for Medical Engineering and Science, Harvard-MIT Division for Health Sciences and Technology, Cambridge, Massachusetts 02139, USA.

[2]School of Engineering and Materials Science, Queen Mary University of London, London E1 4NS, UK.

[3]Grup d'Enginyeria de Materials, Institut Quimic de Sarria-Universitat Ramon Llull, Barcelona 08017, Spain.

[4]Division of Bioconvergence Analysis, Korea Basic Science Institute, Yuseong, Daejeon 169-148, Republic of Korea.

[5]Broad Institute of MIT and Harvard, Cambridge, Massachusetts 02142, USA.

[6]Department of Medicine, Biomedical Engineering Division, Brigham and Women's Hospital, Harvard Medical School, Boston, Massachusetts 02115, USA.

Abstract

The therapeutic potential of miRNA (miR) in cancer is limited by the lack of efficient delivery vehicles. Here, we show that a self-assembled dual-colour RNA-triple-helix structure comprising two miRNAs—a miR mimic (tumour suppressor miRNA) and an antagomiR (oncomiR inhibitor)—provides outstanding capability to synergistically abrogate tumours. Conjugation of RNA triple helices to dendrimers allows the formation of stable triplex nanoparticles, which form an RNA-triple-helix adhesive scaffold upon interaction with dextran aldehyde, the latter able to chemically interact and adhere to natural tissue amines in the tumour. We also show that the self-assembled RNA-triple-helix conjugates remain functional *in vitro* and *in vivo,* and that they lead to nearly 90% levels of tumour shrinkage two weeks post-gel implantation in a triple-negative breast cancer mouse model. Our findings suggest that the RNA-triple-helix hydrogels can be used as an efficient anticancer platform to locally modulate the expression of endogenous miRs in cancer.

[*]Correspondence and requests for materials should be addressed to J.C. or N.A. jdconde@mit.edu; nartzi@mit.edu.

Author contributions

J.C. and N.A. conceived the project and designed the experiments. J.C., N.O., H.S.S. and M.A. performed the experiments, collected and analysed the data. J.C. and N.A. co-wrote the manuscript. All authors discussed the results and reviewed the manuscript.

Competing financial interests

The authors declare no competing financial interests.

Additional information

Supplementary information is available in the online version of the paper.

Fulfilling miRNA (miR) potential in abrogating cancer is challenged by the lack of efficient delivery vehicles capable of releasing miRs to tumour cells[1–5]. Poor miR *in vivo* stability, nonspecific biodistribution, modification of endogenous RNA machinery, and undesired side effects may be overcome by an efficient local and sustained delivery platform. The delivery of miRs has been realized using inorganic nanoparticles (for example, gold, magnetic; refs 6,7), liposomes[8,9] and lipids[10,11], micelles[12], peptide nucleic acids (PNAs; ref. 13), packaging RNA (pRNA; ref. 14) and polymeric[15,16] nanoparticles. However, miR dissociation from the vehicle, low vehicle stability and inefficient targeting, all lead to poor silencing efficiency[17]. Self-assembled three-dimensional structures of oligonucleotides have showed promising applicability for imaging and gene delivery mainly using siRNAs (refs 18–22). DNA triple helices have previously been used either as artificial nucleases or as highly specific repressors, modulating protein recognition of DNA *in vitro* (refs 23–25). However, an RNA-triple-helix assembly for miR delivery or for other *in vivo* applications has not been described before. Here, we hypothesized that the self-assembly of miRs to form a RNA-triple-helix structure would impart high stability and hence improve cancer cells co-transfection efficiency This self-assembled structure was formed by incorporating two therapeutic miRs that form both Watson-Crick and Hoogsteen hydrogen bonds[26,27], thus producing a stable RNA-triple-helix structure for miR delivery. This triple-helix formation induces further stacking within the tertiary structure domain, improving structural stability. The triplex-forming oligonucleotides (TFO) bind antiparallel to the purine-rich strand in RNA, which requires no base protonation and exhibits pH-independent binding[26,28].

To address the limitations associated with current miR delivery vehicles, we developed an RNA-triple-helix structure for modulating the expression of endogenous miRs in cancer *in vivo*. Two miR oligonucleotides forming a triple helix were used for an *in vivo* miR inhibition strategy (antagomiR, a small synthetic ssRNA used to inhibit an oncomiR) and a miR replacement therapy (miR mimic, a mature miR duplex composed of both sense and antisense strands used as tumour suppressor) in an orthotopic triple-negative breast cancer (TNBC) mouse model. TNBC is characterized by a lack of progesterone, oestrogen and HER2 receptors. Thus, TNBC is not responsive to conventional hormonal therapy (such as tamoxifen or aromatase inhibitors) or therapies that target HER2 receptors, such as Herceptin (trastuzumab)[29], which is a biological macromolecule for targeted therapy. Hence, TNBC can benefit from gene therapy approaches, including endogenous miR modulation. When a miR that is upregulated intimately contributes to breast cancer progression (for example, miR-221; ref. 30), an oncogenic miR inhibition therapy can be used to sterically hinder the miR expression via an antagomiR. Additionally, if a miR is downregulated in breast cancer (for example, miR-205; ref. 31), the delivery of mature miRs (miR mimic oligonucleotide with the same sequence as the endogenous mature miR) would restore balanced miR expression levels. We hypothesized that co-delivery of antagomiRs and miR mimics would synergistically abrogate tumours. We further devised that device efficacy would be enhanced if stabilized in a helical structure and protected by an adhesive hydrogel formed *in situ* that coats the tumour. Hence, this study reports on the development of a novel RNA-triple-helix hydrogel scaffold through programmable self-assembly of the two miR sequences to provide a stable and efficient nanovehicle for *in vivo* miR local delivery (Fig. 1a). Conjugating the RNA-triple-helix to dendrimer (triplex nanoparticles) that forms an

adhesive hydrogel upon mixing with dextran aldehyde affords local and controlled release of the two miRs. The RNA-triple-helix structure consists of stable two-pair FRET donor/quencher RNA oligonucleotides able to report on the *in vivo* release of the miRs on conjugation to complementary targets.

Optimization of RNA-triple-helix nanoconjugates/scaffolds

The RNA triplex nanoparticles are formed by complexation of the triple-helix strands (Fig. 1b) with polyamidoamine (PAMAM) G5 dendrimer creating a branched sponge-like nanoscopic structure readily visible using cryo-electron microscopy (cryo-EM, Fig. 1c and Supplementary Fig. 1) and in the high-resolution scanning electron microscope (SEM, Fig. 1d,e and Supplementary Fig. 1) images. Micron-level RNA aggregates (3.4 ± 1.1 μm as measured by SEM, Fig. 1d) are formed by interactions between the RNA triplex nanoparticles (56.6 ± 3.9 nm as measured by SEM, Fig. 1e) and the naked PAMAM G5 dendrimer (5.3 ± 0.7 nm as measured by cryo-EM, Supplementary Fig. 2a,b). The cationic surface of the dendritic system provides an easy platform for attaching RNA via electrostatic interactions between the positively charged terminal amines from PAMAM dendrimers and the negatively charged RNA phosphate. These triplex nanoparticles exhibit densely packed molecular structures (Supplementary Fig. 2c,d) of approximately 50 nm in diameter, which is also confirmed by dynamic light scattering (DLS) analysis revealing a hydrodynamic diameter of 48.4 ± 5.7 nm. Next, we confirmed that the branched sponge-like dendritic structures contain complexed RNA using SYBR green II staining (Supplementary Fig. 2e), a sensitive dye used to detect RNA. The green fluorescence emitted from the RNA triplex nanoparticles confirms that this structure is composed of dendrimer containing RNA. This 3D RNA structure is then allowed to react with dextran aldehyde to form a dextran–dendrimer–RNA triplex hydrogel (Fig. 1f–h) affording local administration of both the carrier and cargo while forming a strong adhesion to the tumour tissue[32,33]. High-resolution SEM images of the hydrogels confirm that the triplex nanoparticles are maintained and dispersed throughout the scaffold following adhesive formation (Fig. 1f–h and in Supplementary Fig. 3a–f).

Therefore, this self-assembled platform provides control over multiple length scales: RNA triplex assembly at the nanoscale (small dendrimer triplex nanoparticles, ~50–60 nm, Fig. 1e), dendrimer–triplex complexation followed by their aggregation at the microscale (~3–4 μm, Fig. 1d), and adhesive hydrogel formation following dextran addition at the macroscale (>1 mm, Fig. 1f–h).

The dual-colour RNA triple helix was constructed using three strands of RNA oligonucleotides, denoted as miR-205 sense, antisense and antagomiR-221 (RNA oligomers sequences are depicted in Supplementary Table 1). The miR-205 sense comprises a 28 nt RNA oligo double-modified with a Black-Hole dark quencher (BHQ2) at the 5′ end and a cholesterol molecule at the 3′ end. The latter neutral lipid was used to facilitate the permeation of cell membranes, improve co-transfection efficiency *in vivo* and protect oligonucleotides from degradation[34]. The miR-205 antisense comprises a28 nt RNA oligo modified with a near-infrared (NIR) dye, Quasar 705 (Q705), at the 3′ end. The antagomiR-221 represents a 30 nt RNA oligo modified with a Quasar 570 (Q570) at the 3′

end. The absorbance spectra of RNA oligonucleotides alone and conjugated to form the double and triple helices are depicted in Supplementary Fig. 4. The triplex design affords quenching effects between the dye/quencher pair, indicating the specific spatial proximity of the three RNA oligonucleotides composing the 3D structure and, consequently, the formation of the triple-helix assembly.

To verify the RNA-triple-helix formation and determine the optimal molar ratio between the three oligonucleotides, the fluorescence intensity of the RNA oligonucleotides (two double-helix- or triple-helix-forming structures) with graded molar ratios was measured at room temperature using a live imaging system (Fig. 2a). A nearly 100% quenching effect (no fluorescence emission) induced by the proximity of the chromophores with the quencher BHQ2 can be observed at a 1:1:1 molar ratio or higher. The emission spectra of these samples are depicted in Supplementary Fig. 5 and the region of interest (ROI) quantification of the Q570 and Q705 channels for several molar ratios are shown in Supplementary Fig. 6.

Efficient formation of the triple helix composed of the three oligonucleotides—miR-205 sense and antisense and antagomiR-221 (Fig. 2b)—occurs at a 1:1:1 molar ratio at room temperature in incubation buffer, 10 mM Tris buffer (pH 7) supplemented with 10 mM $MgCl_2$, 1 mM spermine and 0.8 mM of $CuSO_4$. The copper ions were introduced to favour the intercalation of the nitrogen atoms in the minor groove of the triplex where copper binding occurs[35].

Successful self-assembly of the RNA triple helix (lane 7) was also confirmed using gel electrophoresis at 25 °C, as seen by the slower migration rates compared with the two double helices (lanes 4 and 5) and with the single RNA oligonucleotides (lanes 1–3) (Fig. 2c).

To ensure proper triplex function *in vivo*, triplex stability was examined under (pre)clinically relevant conditions, including temperature, pH, and in the presence of urea, which is capable of denaturing and dissociating dsRNAs. RNA oligonucleotides melting temperature (T_m) was examined in the triplex form (T_m = 74.5±3.2 °C), the ssRNA oligonucleotides alone (T_m = 55.1 ± 1.9 °C) and the double-helix form; miR-205 sense and antisense (T_m = 63.1 °C) and miR-205 sense and antagomiR-221 (T_m = 64.8 ± 2.6 °C) (Fig. 2d). The shift in T_m of the triplex to 75 °C points at a highly stable structure.

Extensive and meticulous characterization of the triplex formation was performed using several competition assays (see Supplementary Information), such as ionic strength[36,37] (Supplementary Fig. 7), temperature profiles (Supplementary Fig. 8), urea stability38 (Supplementary Fig. 9), serum stability (Supplementary Fig. 10) and pH (Supplementary Fig. 11). These results corroborate the high stability of the triplex in the presence of ultralow concentrations of magnesium, at high temperatures (that is, 65 °C), in physiological and super-physiological concentrations of urea, in long exposure to 50% serum and in a pH range of 5–9.

To ensure triplex *in vivo* recognition by the transcriptional machinery following miR strands intracellular delivery, triplexes were incubated with recombinant human Dicer and AGO2/EIF2C2 enzymes (Supplementary Fig. 12). These enzymes are responsible for the

recognition and unwinding by RISC and by the Argonaute protein family (specially, AGO2; ref. 39). The RNA-triple-helix oligonucleotides were recognized and cleaved into smaller RNA products only in the presence of recombinant AGO2, when compared to the RNA triple helices without AGO2 treatment. Hence, the strong RNA-triple-helix recognition by AGO2 depicts the self-assembled RNA triple helix as a highly specific structure.

To verify dendrimer–triplex complex formation, an electrophoretic mobility shift assay (EMSA) was performed on agarose gel using increasing concentrations of PAMAM G5 (0.01–5 mg ml^{-1}), pre-incubated with 1 μM of the RNA triple-helix (Supplementary Fig. 13a). Indeed, a substantial change in the electrophoretic mobility of RNA triple helix complexed with PAMAM G5 is evident for dendrimer concentrations higher than 0.025 mg ml^{-1}, pointing at successful complexation. Whereas PAMAM G5 alone imparts cytotoxicity in a dose-dependent manner (0.1–5 mg ml^{-1}) (Supplementary Fig. 13b), its complex with RNA triplex or control triplex is cyto-compatible even at high dendrimer concentrations.

Cellular internalization of RNA-triple-helix nanoconjugates

We next studied the cellular uptake of the complex PAMAM G5 dendrimer (Mr. 28 kDa) with the RNA oligonucleotides using the MDA-MB-231 TNBC cell line. With an extraordinary cellular uptake efficiency, analytical flow cytometry data showed that RNA triplex nanoparticles (0.05 mg ml^{-1} of dendrimer complexed with 1 μM of triplex oligonucleotides) were able to transfect nearly 100% (99.8 ± 2.5%) of the cancer cells with a strong and uniform signal from both dyes (Q705 and Q570) (Fig. 2e). The RNA–dendrimer complexes could accumulate in MDA-MB-231 cells, as verified by confocal microscopy at 24 h (Fig. 2f). Confocal imaging showed efficient uptake of the RNA–dendrimer into targeted cells, as demonstrated by the outstanding co-localization and overlap of the dual-colour RNA triple helix at 24 h (Fig. 2f). Confocal images of cellular uptake kinetics for cells incubated with RNA triplex nanoparticles for 0.5, 3, 6, 24 and 48 h are depicted in Supplementary Fig. 14, showing that the triplex nanoparticles are internalized by cells at 3 h with a maximum peak of cellular uptake at 48 h. The evaluation of cellular uptake was also performed following the administration of both RNA double helices separately (Supplementary Fig. 15). However, flow cytometry and confocal data reveal only moderate uptake efficiency of 38% (38.3 ± 7.6%) for each of the RNA double helices when provided separately, when compared to the excellent uptake of the triple helix (99.8 ± 2.5%), confirming that co-transfection with RNA triple helix is far more efficacious. Higher triplex efficacy is a result of improved triplex stability. Furthermore, the dendrimer amine binding groups available for interaction with the double or triple helices are finite, hence a higher ‘effective’ amount of each sequence will be complexed to the dendrimer surface when in a triplex structure.

Uptake mechanism of RNA-triple-helix nanoconjugates

It is well known that nanoparticles utilize different endocytosis mechanisms for cellular uptake. Generally, endocytosis can be divided into macropinocytosis, clathrin-dependent endocytosis and caveolae-mediated endocytosis[40]. To decipher the uptake mechanism of the triplex–dendrimer compared to naked dendrimer, we utilized molecules capable of inhibiting

each of these cellular pathways at a time. The endocytosis inhibitors used were chlorpromazine, filipin, rottlerin, brefeldin A, colchicine and chloroquine, whose endocytic function and structure can be found in Supplementary Fig. 16.

In the absence of small-molecule inhibitors, the naked PAMAM dendrimer (labelled with Alexa Fluor 594, Fig. 3a) and the dendrimer complexed with triplex oligonucleotides (0.05 mg ml^{-1} of dendrimer complexed with 1 μM of oligonucleotides, Fig. 3b), co-localization within the lysosomes at 0, 3, 6, 24 and 48 h after exposure was studied. The co-localization of naked dendrimer with the lysosomes is more evident than the dendrimer complexed with triplex oligonucleotides and decreases with time, which is consistent with the accumulation of PAMAM dendrimer in lysosomes and with dendrimers' capability to escape the endosome via the 'proton-sponge effect'. Here the 'proton-sponge effect' occurs when unprotonated dendrimers absorb protons as they are pumped into the lysosome, resulting in more protons being pumped in, leading to an increased influx of Cl^- ions and water, resulting in swelling and rupture of the lysosomal membrane with subsequent release into the cytoplasm[41]. At 48 h, the naked dendrimer was almost completely recycled—that is, trafficking to the extracellular milieu has occurred as evident by the marked decrease in fluorescence signal (Fig. 3a). However, when the dendrimer is complexed with the RNA triple helix the co-localization of these particles with the lysosomes is no longer evident even after 48 h of incubation (Fig. 3b). It seems that these nanoconjugates do not strongly co-localize with lysosomes like the naked dendrimers, suggesting that they might enter cells via a different uptake mechanism.

In the presence of small-molecule inhibitors, the internalization and sub-cellular localization of naked dendrimers and triplex–dendrimer nanoparticles was visualized by confocal microscopy (Fig. 3c,e) and quantified by analytical flow cytometry (Fig. 3d,f). A significant reduction in naked PAMAM dendrimer uptake and permeability was observed in the presence of the endocytosis inhibitors filipin (blocks caveolae endocytosis) and brefeldin A (Fig. 3c). Filipin reduced naked PAMAM uptake by 94.2 ± 2.7% and brefeldin A reduced the uptake by 92.2 ± 2.5% (Fig. 3d). These findings support previous results that naked cationic dendrimers like PAMAM are endocytosed[42] probably via caveolae endocytosis.

Interestingly, when dendrimer is complexed with the RNA-triple-helix oligonucleotides to form the triplex nanoparticles the uptake mechanism changes completely. Now, a significant reduction in uptake and permeability was observed in the presence of the macropinocytosis inhibitors rottlerin and colchicine (also microtubules inhibitor) (Fig. 3e). Rottlerin reduced triplex nanoparticles uptake by 78.6 ± 2.1% and colchicine reduced the uptake by71.1 ± 1.5% (Fig. 3f). Macropinocytosis is usually initiated by extensive plasma membrane reorganization or ruffling to form an external macropinocytic structure that is then enclosed and internalized[43]. As macropinocytosis is dependent on microtubule function, and these structures are implicated in plasma membrane ruffling[44], colchicine that interferes with microtubule trafficking through binding to tubulin subunits, uptake of triplex (Fig. 3e,f) and control triplex (Supplementary Fig. 17) nanoparticles was significantly reduced. In summary, naked dendrimers and triplex–dendrimers utilize completely different mechanism to enter the cells. Whereas naked PAMAM dendrimers utilize endocytosis to enter cells and

bypass the lysosomes, the triplex–dendrimer nanoconjugates utilize micropinocytosis, probably by triggering actin-mediated membrane ruffling.

This difference in uptake mechanisms is highly dependent on the particles' physicochemical characteristics[45]. Properties such as size and charge are ascertained to influence the endocytosis of these kind of nanomaterials. Zeta potentials of naked PAMAM dendrimer (+52.7 ± 1.5 mV) and dendrimer–triplex nanoparticles (−19.6 ± 4.6 mV) revealed that naked dendrimers are highly cationic, whereas when complexed with the RNA triple helix they are slightly anionic. Usually the cationic particles strongly interact with the membrane and enter cells rapidly, whereas anionic particles can enter cells by binding to the positive site of the membrane[45]. Moreover, the size of these nanoconjugates is also significantly altered. The dendrimer–triplex assembly structures size is 48.4± 5.7 nm in diameter (as measured by DLS) and their aggregation occurs at the microscale (3.4 ± 1.1 μm as measured by SEM, Fig. 1d), whereas the naked dendrimer size is only 6.7 ± 0.4 nm in diameter as measured by DLS and 5.3 ± 0.7 nm as measured by cryo-EM (Supplementary Fig. 2a,b). In fact, nanoparticles larger than 1 μm are most likely to be engulfed via macropinocytosis, whereas the size involved in caveolae-mediated endocytosis is about 60–80 nm (ref. 40), all consistent with the dendrimer–triplex microstructure and the naked dendrimer sizes.

Impact of miRs delivery on breast cancer cells' phenotype

The impact of miRs delivery on cancer cells was evaluated. We first confirmed the reduction in miR-221 (oncogenic) expression level and enhancement ofmiR-205 expression (tumour suppressor) following treatment with the RNA triple helix compared with the control triple helix (triplex formed with scrambled miR sequences) after 24, 48 and 72 h of incubation (Fig. 4a). To corroborate these results, a luciferase reporter was constructed to assess RNA triplex nanoparticles activity, which proves the functional role of altering the expression of the studied miRNAs in abrogating cancer (Supplementary Fig. 18).

We then proceeded to examine the phenotypic effects of miR replacement and oncomiR inhibition via a RNA-triple-helix vehicle in tissue culture. Hence, the tumorigenicity of MDA-MB-231 cells was evaluated by measuring the half maximal inhibitory concentration (IC_{50}) via a MTT assay (Fig. 4b), cell migration/proliferation via a wound closure assay (Fig. 4c), and cell growth and viability using a clonogenic survival assay with crystal violet (Fig. 4d,e) following treatment with RNA-dendrimer complexes (0.05 mg ml^{-1} of dendrimer complexed with 1 μM of triplex oligonucleotides). RNA triple helices significantly inhibited the growth of MDA-MB-231 cells compared with the two double helices (Q570 and Q705), and with a control triplex (Fig. 4b).

Cell migration and proliferation were studied using a wound closure assay where cells were allowed to grow in a 24-well plate until confluency and a wound was created using a sterile pipette tip. The cells were then incubated with the RNA–dendrimer complexes and wound closure was monitored using light microscopy. Cells treated with a control triplex were able to close the wound almost completely (~90%) within 72 h (Fig. 4c and Supplementary Fig. 19). Cells treated with the two double-helix miRs separately showed a partial closure of the wound over this time frame (75% for Q570 and 35% for Q705 oligonucleotides), whereas

cells treated with the RNA triple helix were not able to close the wound at all. These data indicate that the delivery of both mimic miR-205 and antagomiR-221 almost completely eliminates the motility of MDA-MB-231 cells (Fig. 4c). A remarkable reduction in cell survival of about 95% following RNA-triple-helix delivery was observed after 72 h of incubation using a clonogenic survival assay, when compared with a control triplex (Fig. 4d,e and Supplementary Fig. 19).

Taken together, these data confirm that the dual miR delivery provided by the RNA triple helix for the replacement of the miR-205 and the inhibition of the miR-221 exploit endogenous pathways to exert the desired phenotypic response of breast cancer cells, controlling the cell migratory behaviour.

Characterization of RNA-triple-helix hydrogel scaffolds

We hypothesized that efficacious delivery of the RNA-triple-helix hydrogel nanoconjugates would be achieved by coating the breast tumour with the adhesive hydrogel scaffold[33] that we have previously shown able to enhance the stability of embedded nanoparticles used for local gene delivery[32,46]. A fluorescent image of the dual-colour RNA triple helix in the form of a hydrogel scaffold is depicted in Fig. 5a. Epi-fluorescence images following hydrogel cryo-sectioning show a distinct and punctuate signal from the RNA-triple-helix nanoparticles throughout the hydrogel network (Fig. 5b). The RNA-triple-helix hydrogel nanoconjugates that were pre-incubated with the complementary target for both strands show a positive fluorescence signal, whereas the ones without target do not show any fluorescence signal from the triple helix. This confirms that individual RNA-triple-helix modules complexed with the hydrogel network retained their original folding (Supplementary Fig. 20). Triple-helix nanoparticles (1 μM of RNA oligonucleotides complexed with 5% PAMAM G5 dendrimer) were mixed with 5% dextran aldehyde to form a hydrogel to a total of 12.5% dendrimer amine. RNA-triple-helix hydrogel scaffolds showed high triplex stability, with a complete discharge release within 24 to 48 h (Supplementary Fig. 21).

In vivo miRNA modulation via RNA-triple-helix scaffolds

Next, we proceeded to study the *in vivo* nanoconjugates pharmacokinetics and platform therapeutic efficacy in an orthotopic breast cancer mouse model. The efficacy of our gene-therapy-based therapeutic platform was compared to chemotherapy drugs that are part of the current standard of care for human breast cancer, including doxorubicin (DOX; ref. 47), paclitaxel (PTX; ref. 48) and the monoclonal antibody bevacizumab (Avastin)[49].

Hydrogel scaffolds loaded with the RNA oligonucleotides (1 μM of RNA oligonucleotides doped in 5% PAMAM G5 dendrimer) or drugs (at final concentration: DOX = 0.8 μM; PTX = 300 μM; Avastin = 0.07 μM, see Supplementary Fig. 22) were implanted adjacent to the tumour in the mammary fat pad of SCID hairless congenic mice when tumours reached a desired volume of ~100 mm^3. Inhibition of tumour progression was measured by luciferase expression while each RNA oligo release was tracked fluorescently (Fig. 5c) via a live imaging system for two weeks post-hydrogel implantation. No signs of inflammation were

observed at the surgical site and no changes in body weight were observed before or after breast tumour induction or hydrogel implantation (Supplementary Fig. 23), suggesting that hydrogels are biocompatible with no associated toxicity or side effects. Bioluminescence imaging of mice (Fig. 5c) and tumour size measurements (Fig. 5f) revealed that only the RNA-triple-helix hydrogel scaffolds (that carry the mimic miR-205 and the antagomiR-221) were able to promote efficient and sustained inhibition of tumour progression, with almost 90% tumour size reduction ($n = 5$, $P < 0.001$) 13 days after hydrogel disk implantation. Conversely, 50% tumour reduction was attained following each miR administration separately (Supplementary Figs 24–26), whereas hydrogel only, control triplex (scrambled miRs) and Avastin-loaded hydrogel showed no tumour size reduction. DOX- and PTX-loaded hydrogels showed a 25% and 35% reduction in tumour size, respectively.

In fact, treatment with drug-loaded hydrogels revealed that at early time points (1 to 3 days) the administration of DOX and PTX significantly reduced the onset of tumour progression (as judged by tumour size in Fig. 5f and *in vivo* luciferase signal in Supplementary Fig. 27a,c). However, this reduction was temporary and diminished as the tumour continued to grow. In fact, traditional chemotherapeutic agents are often associated with the recurrence of tumour after several days of treatment, requiring multiple administrations, which is consistent with the results presented here. The high efficacy following miR delivery stems from the selective and specific delivery to tumour cells only compared with the nonselective chemotherapeutic drug uptake. In fact, our strategy of inhibiting an oncogenic miR-221 and providing a tumour suppressor miRNA (miR-205) simultaneously leads to a potent and long-lasting tumour inhibition.

RNA nanoconjugates uptake and biodistribution were examined by quantifying fluorescence images of mice organs (liver, kidneys, spleen, heart, lungs and intestines) 13 days post-implantation (treatment groups in Fig. 5c, control groups in Supplementary Figs 24–26). At 13 days, 20–30% of the miRs persist in the tumoral tissue exclusively (Fig. 5c), when compared to major organs. No fluorescence signal was found in any of the major organs. A time curve documenting the triplex signal (Q705 and Q570 dyes) in organs harvested from mice treated with the RNA-triple-helix hydrogel scaffolds for 2, 6, 24, 48, 72 h and days 5, 8, 11 and 13 is depicted in Supplementary Fig. 28. The triplex nanoparticles accumulate exclusively in the tumour tissue, as demonstrated by the *ex vivo* images of the organs (Supplementary Fig. 28b) and time curve for each organ (Supplementary Fig. 28c,d). There is no accumulation of the triplex nanoparticles in any major organ in any of the time points during the 13 days, except some background signal in the intestine (also observed at 0 h of incubation).

Intriguingly, we found staggered release kinetics of the two miRs. The maximum fluorescence peak occurs at 24 h for the tumour suppressor miR-205 and only at 48 h for the antagomiR of the miR-221 (Supplementary Figs 25 and 26). This staggered kinetics suggests that the miR-205 is initially processed by the RISC complex and by Ago2 and then the antagomiR. Taken together, these results prove that our system is able to initially enhance the expression of a tumour suppressor miR and 24 h later to inhibit the oncogenic miR responsible for breast tumour progression and proliferation. Our data confirm the

capacity of this platform to provide efficient *in vivo* miR replacement therapy and to promote oncogenic miR inhibition.

H&E staining of breast tumour sections showed evidence of extensive reduction in vascularization for mice treated with RNA-triple-helix scaffold (Fig. 5d), when compared to control triplex, in accordance with tumour size reduction due to miRNAs delivery to the tumour microenvironment. An increasing number of large blood vessels can be found in the control triplex groups (Fig. 5d). Immunohistochemical analysis showed that the expression of Ki67, a cellular marker strictly associated with cell proliferation, was reduced only after treatment with hydrogels embedded with RNA-triple-helix nanoparticles (Fig. 5e).

A survival study was performed for mice treated with hydrogel scaffolds loaded with the triplex and control triplex, as well as for the chemotherapeutic drugs (DOX, PTX and Avastin) (Fig. 5g). Mice implanted with RNA-triple-helix hydrogel scaffolds showed a highly significant survival advantage ($P = 0.006$) compared with hydrogel only, with control triplex hydrogels and with drug-loaded hydrogels (Fig. 5g). Survival correlates with the significant tumour size reduction observed mainly in mice treated with RNA-triple-helix hydrogel scaffolds (Fig. 5f).

Following miR delivery, we investigated the tumour genetic expression profile of *LAMC1, E2F1* and *p53* (regulated by miR-205) and *E-cadherin, Snaill* and *Slug* (*Snail2*) (regulated by miR-221). These key genes are major regulators of cell cycle progression (*E2F1*), tumour suppressor (*p53*) or major components of extracellular matrix involved in cell adhesion, proliferation and migration (*LAMC1, E-cadherin, Snaill* and *Slug*). The heat-map depicts qPCR analysis of RNA extracted from resected tumours (Fig. 5h). Quantitative PCR determination of gene expression levels in mice treated groups for all the studied genes can be found in Supplementary Fig. 29. This genetic screening shows that miR-205 directly targets *LAMC1*, a protein altered in human breast cancer that has been implicated in a wide variety of biological processes, including cell adhesion, differentiation, proliferation, migration, signalling and metastasis[31]. When miR-205 expression is enhanced by the triple-helix scaffold, the expression of *LAMC1* decreases considerably, altering cancer cells proliferation, as corroborated by our *in vitro* (Fig. 4) and *in vivo* data (Fig. 5). miR-205 also directly targets *E2F1,* a gene that is overexpressed in triple-negative breast tumours[31], in which the level of miR-205 is low. We found that increasing the miR-205 expression by the delivery of RNA-triple-helix scaffolds substantially decreases the expression of *E2F1.* Hence, these results demonstrate that *E2F1* is a target of miR-205 in triple-negative breast cancer tissues. Interestingly, *p53* acts like an enhancer of miR-205 expression, as the increase in the expression of this miR is followed by the upregulation of *p53* (Fig. 5h). miR-221 expression, which is found to be upregulated in triple-negative breast tumours (Fig. 5h) and in a panoply of cancer types[30], has been shown to directly target proliferation and adhesion genes, such as *E-cadherin, Snail1* and *Slug* (*Snail2*). We found that the inhibition of miR-221 alters *E-cadherin* expression and its regulatory transcription factors *Snail* and *Slug* with a corresponding strong reduction in cell migration and invasion in breast tumours. Downregulation of miR-221 increases *E-cadherin* levels and decreases the expression levels of *Snail* and *Slug* (Fig. 5h). Moreover, the expression of *VEGF* is highly downregulated, in particular in mice treated with RNA-triple-helix scaffolds, where the inhibition of tumour

size is more significant (Fig. 5c,f). Taken together, these gene expression data validate the ability of the RNA-triple-helix scaffold to inhibit oncogenes and to enhance immunosuppression capacity, resulting in efficient tumour reduction of nearly 90%, achieved only following dual miR therapy (Fig. 5f).

Outlook

We report herein on a novel strategy for concomitant oncomiR inhibition and tumour suppressor miR replacement therapy using a RNA-triple-helix hydrogel scaffold that affords highly efficacious local anticancer therapy. Self-assembled RNA-triple-helix conjugates remain functional *in vitro* with high selective uptake and control over miR expression compared to their respective single-stranded or double-stranded forms. Hence, cancer gene delivery systems should provide potent, selective and specific treatment to tumour cells only, unlike the standard delivery of most conventional chemotherapeutic drugs. This approach can be implemented to design self-assembled triplex structures from any other miR combination, or from other genetic materials, including antisense DNA or siRNA, to treat a range of diseases.

Methods

Methods and any associated references are available in the online version of the paper.

Methods

Preparation of self-assembled RNA triple helix

The dual-colour RNA triple helix was constructed using three pieces ofRNA oligonucleotides (Biosearch Technologies Inc.), denoted as miR-205 sense and antisense and antagomiR-221. The miR-205 sense comprises a 28 nt RNA oligo double-modified with a Black-Hole dark quencher (BHQ2) at 5′ and a cholesterol molecule at 3′, and the miR-205 antisense comprises a 28 nt RNA oligo modified with a NIR dye, Quasar 705, at the 3′. The antagomiR-221 represents a 30 nt RNA oligo modified with a Quasar 570 at the 3′. Scrambled miRs (Biosearch Technologies) synthesized with the same modifications and dyes were used to form a control triple helix. The three RNA strands were mixed in an equal molar ratio (1:1:1, final concentration 1 μM each) or several combination ratios at room temperature in incubation buffer: 10 mM Tris buffer pH 7 (Bio-Rad) supplemented with 10 mM $MgCl_2$ (Sigma), 1 mM spermine (Sigma) and 0.8 mM of $CuSO_4$ (Sigma), and then heated up to 80 °C for 5 min and rapidlycooled to 4 °C.

Characterization and competition assays

Presence of urea—The concentration of single RNA and the RNA-triple-helix oligonucleotides (equal molar ratio 1:1:1, final concentration 1 μM each) was fixed and the samples were loaded on 20% TBE PAGE gel without and with urea (0.007 and 7M) (Invitrogen).

Different temperatures and melting experiments—The three RNA strands were mixed in an equal molar ratio (1:1:1, final concentration 1 μM each) and were incubated for

30 min at 25, 37 and 65 °C and then loaded onto a 20% TBE gel (Invitrogen). Melting experiments were conducted by monitoring the fluorescence of the SYBR Gold (Invitrogen) intercalated-RNAs using a Light Cycler 480 II Real-time PCR machine (Roche). Briefly, 1 × SYBR Gold dye (Excitation/Emission = 495/537 nm, Invitrogen), which is 25–100 times more sensitive than ethidium bromide and detects dsRNA, ssRNA and DNA. The single RNA and the RNA-triple-helix oligonucleotides (equal molar ratio 1:1:1, final concentration 1 μM each) were mixed at room temperature in incubation buffer. The RNA samples were slowly cooled from 95 to20 °Cata rate of 0.11 $°Cs^{-1}$. Data were analyzed with a Light Cycler 480 II Real-time PCR machine software using the first derivative of the melting profile. The first derivative of the melting temperature is calculated as follows: dRFU/dT, with RFU being the relative fluorescence units (from the SYBR Gold) and T the temperature (in Celsius) for each cycle of measurement. The first derivative of this function tells us howwhether the temperature is increasing or decreasing, and by how much it is increasing or decreasing. In other words, for each temperature point, the average value of a reference curve is calculated and subsequently subtracted from each sample's normalized *RFU* value to generate a difference plot. Consequently, a vertical shift in fluorescence intensity on the *y*-axis, following reference signal subtraction, is used to identify temperature profile differences. The T_m value represents the mean and standard deviation of three independent experiments.

Different pHs—The concentration of single RNA and the RNA-triple-helix oligonucleotides in equal molar ratio (1:1:1, final concentration 1 μM each) was fixed and the samples were incubated with different pH solutions (from 3 to 12) for 30 min and then loaded on 20%TBE gel (Invitrogen).

Stability assay in serum—The single RNA and the RNA-triple-helix oligonucleotides were incubated in 50% fetal bovine serum (Gibco). A sample ofRNA was taken at 0, 5, 10, 24, 48 and 72 h time points after incubation at 37 °C, followed by analysis using 20% TBE gel (Invitrogen).

Quenching/Fluorescence assays—The RNA strands were mixed in an equal molar ratio (1:1:1, final concentration 1 μM each) or at several combination ratios at room temperature in incubation buffer and then heated up to 80 °C for 5 min and rapidly cooled to 4 °C. After this, fluorescence spectra were taken using a microplate reader (Varioskan Flash Multimode Reader, Thermo Scientific) and fluorescence images taken using the IVIS Spectrum-bioluminescent and fluorescent imaging system (Xenogen XPM-2 Corporation). The Quasar570 has an Excitation/Emission at 548/570 nm and the Quasar705 at 690/705 nm.

Specifity assay with recombinant Dicer and Ago2—For the recognition of miRs and the concomitant dissembly of the RNA triple helix by the Dicer and Ago2 proteins, the RNA triple helix was previously incubated in an equal molar ratio 1:1:1, final concentration 1 μM of each oligo to form the structure. For DICER specificity assay, increasing amounts of recombinant human Dicer (Genlantis) from 0.5 to 2 units were incubated with 1 μM of the triple-helix oligonucleotides for 16h at 37 °C and then collected and inhibited by adding

Dicer stop solution (Genlantis). The samples were then run on a 20% TBE gel (Invitrogen) to evaluate the by-products of the reaction. For Ago2 assay, increasing amounts of recombinant human AGO2/EIF2C2 (Sino Biological) from 5 to 160 ng were incubated with 1 μM of the triple-helix oligonucleotides for 60 min at 37 °C. Reactions were stopped by incubation at 65 °C for 30 min. The samples were then run on a 20% TBE gel (Invitrogen) to evaluate the by-products of the reaction.

General characterization of the self-assembled RNA triple helixwas performed by dynamic light scattering (DLS; Wyatt Dyna Pro Plate Reader), zeta potential (Zetasizer Nano-ZS90 Malvern), fluorescence and ultraviolet/visible spectroscopy and high-resolution SEM (Zeiss Merlin High-resolution SEM, EHT = 3.00 kV, I Probe = 80 pA, Signal A = InLens or HE-SE2) and high-resolution Cryo-TEM (JEOL2100 FEG TEM).

In vitro RNA-triple-helix–dendrimer nanoconjugates delivery

MDA-MB-231 triple-negative breast cancer cells (ATCC Cat. No. HTB-26, tested for mycoplasma contamination bythe Division of Comparative Medicine Diagnostic Lab atMIT via IMPACT PCR, which was negative) were grown in Dulbecco's modified Eagle's medium (DMEM, Invitrogen) supplemented with 4 mM glutamine, 10% heat-inactivated fetal bovine serum (Gibco, Life Technologies), 100 U ml^{-1} penicillin and 100 μg ml^{-1} streptomycin (Invitrogen) and maintained at 37 °C in 5% CO_2. Cells were seeded at a density of 1×10^5 cells/well in 24-well plates and grown for 24h before incubation of RNA–dendrimer nanoconjugates (0.05 mg ml^{-1} of dendrimer complexed with 1 μM of triplex oligonucleotides). On the day of incubation, the cells were approximately 50% confluent. For confocal microscopy, cells were fixed with 4% paraformaldehyde in PBS for 15 min at 37 °C, stained with DAPI to allow nuclear staining and finally mounted in ProLong Gold Antifade Reagent (Invitrogen). Images of cells were taken with a Nikon A1R Ultra-Fast Spectral Scanning Confocal Microscope.

Lysosomal staining

To track the intracellular co-localization ofPAMAM dendrimer alone, and the RNA-triple-helix–dendrimer nanoconjugates within lysosomes, Lysotracker Blue was used to label these structures. Briefly, cells were seeded at a density of2×10^5 cells/well in 24-well plates and grown for 24 h prior to incubation of RNA–dendrimer nanoconjugates (0.05 mg ml^{-1} of dendrimer complexed with 1 μM of triplex oligonucleotides). During the final 30 min of the incubations with the RNA–dendrimer nanoconjugates, the lysosomal dye Lysotracker Blue DND-22 (Invitrogen) was included at a final concentration of 500 nM. Then, cells were fixed with 4% paraformaldehyde in 1× PBS for 15 min at 37 °C. Finally, cells were mounted in ProLong Gold Antifade Reagent (Invitrogen). Images of cells were taken with a Nikon A1R Ultra-Fast Spectral Scanning Confocal Microscope.

Uptake mechanism of the RNA-triple-helix–dendrimer nanoconjugates

To evaluate the uptake mechanism of the RNA triple-helix–dendrimer nanoconjugates, cells were treated with several internalization inhibitors. Briefly, cells were seeded at a density of 2×10^5 cells/well in 24-well plates and grown for 24h before incubation of inhibitors and RNA–dendrimer nanoconjugates. Cells were then treated with chlorpromazine (10 μg ml^{-1}),

filipin (5 μg ml^{-1}), rottlerin (10 μM), brefeldin A (5 μM), colchicine (10 μM) or chloroquine (10 μM) (all from Sigma) in normal culture medium for 60 min at 37 °C. Subsequently, PAMAM dendrimer alone (0.05 mg ml^{-1}) and RNA-triple-helix-dendrimer nanoconjugates (0.05 mg ml^{-1} of dendrimer complexed with 1 μM of triplex oligonucleotides) were added and incubation was continued for 3 h. Subsequently, images of cells were taken with a Nikon A1R Ultra-Fast Spectral Scanning Confocal Microscope and the cells were analysed by flow cytometry (FACS).

Flow cytometry

MDA-MB-231 cells incubated with naked PAMAM G5 dendrimer alone or RNA oligonucleotides complexed with PAMAM G5 dendrimers were washed with PBS and detached with 0.25% trypsin-EDTA (Life Technologies). FACS running buffer (500 μl), consisting of 98% PBS and 2% heat-inactivated fetal bovine serum (Gibco, Life Technologies), was added to each well. Cells were mixed thoroughly and then transferred to the FACS tube with a filter lid, and the Alexa Fluor 594 signals (for naked dendrimer) and Q705 and Q570 signals (for triplex) were acquired on a FACS LSR Fortessa HTS-1 (BD Biosciences) flow cytometer.

Luciferase reporter to access nanoconjugates activity

For dual luciferase reporter experiments, the miRNA sensor was generated by inserting the antisense sequence to miR-205 or the sense sequence to miR-221 into the 3′ untranslated region of luciferase on the vector. These cloning vectors were produced by Cyagen Biosciences. The vectors were constructed in *Escherichia coli Stbl3* host to ensure sequence stabilitywith ampicillin as the antibiotic resistance marker (the vector maps can be found in Supplementary Fig. 18). The *E. coli* transformed with the vectors were grown in Luria-Bertani (LB) broth (Invitrogen) supplemented with 100 μg ml^{-1} of ampicillin (Invitrogen) at37 °C overnight. After this, the vectors were extracted and purified from the cultured *E. coli* using aPlasmidMidi Kit (Qiagen). For vector transfection in human breast cancer cells, MDA-MB-231 cells not expressing luciferase were stably transfected with miR-Luc-vectors (1 μg per well) using Lipofectamine 3000 (Invitrogen) according to manufacturers' protocol. Cell lysates were measured with 150 μg ml^{-1} of D-luciferin (Caliper LifeSciences) for luciferase activity after 48 h of luciferase vectors transfection. Then cells were incubated with increasing amounts of the RNA-triple-helix–dendrimer nanoconjugates and controls for 24, 48 and 72 h and the optimal sensor activity was evaluated by a fluorescent imaging system (Xenogen XPM-2 Corporation) and quantification of cell lysate luminescence using a microplate reader (Varioskan Flash Multimode Reader, Thermo Scientific).

Cell viability and proliferation assays

A standard MTT [3-(4,5-dimethylthiazol-2-yl)-2,5-diphenyltetrazoliumbromide] reduction assay (Molecular Probes, Life Technologies) was performed to determine the viability of cells to increasing concentrations of PAMAM G5 dendrimer alone and when complexed with RNA oligonucleotides. Cells were seeded at a density of 1×10^5 cells per well in 24-well culture plates in complete DMEM (500 μl) with serum. After 24 h of exposure to dendrimer with and without RNA oligonucleotides, the medium was removed, the cells were washed twice with sterile PBS, and 300 μl of fresh medium with serum was added. Then

16.7 μl of sterile MTT stock solution (5 mg ml^{-1} in PBS) was added to each well. After incubation for a further 2 h, the medium was removed and the formazan crystals were resuspended in 300 μl of dimethyl sulphoxide (Sigma). The solution was mixed and its absorbance was measured with 540 nm as the working wavelength and 630 nm as the reference wavelength using a microplate reader (Varioskan Flash Multimode Reader, Thermo Scientific). The cell viability was normalized to that of cells cultured in the culture medium with PBS treatment.

For the wound closing assay (frequently used for evaluating migration rates of cells in culture), MDA-MB-231 cells were grown to >95% confluency in a 24-well plate and a wound was made using a sterile pipette tip. The cells were then incubated with the RNA–dendrimer complexes and the wound closure was monitored using light microscopy.

In the clonogenic survival assay, at 24 h after transfection, MDA-MB-231 cells were harvested and resuspended in the culture medium. In 24-well plates, 1×10^5 cells/well were seeded and allowed to grow until visible colonies formed (six days). Cell colonies were fixed using 4% paraformaldehyde (Sigma) for 5 min at 37 °C and stained with 0.05% crystal violet (Sigma) in Mili-Q water filtered with a 0.45 μm filter at room temperature for 30 min. Cell colonies were then washed three times with water and incubated in a half of the total well volume of methanol (Sigma) to solubilize the dye. Then, the absorbance at 540 nm was measured using a microplate reader (Varioskan Flash Multimode Reader, Thermo Scientific). Each sample had three replicates to determine the mean ± s.d.

Quantitative PCR for miRNA expression

Total RNA from MDA-MB-231 cells and breast tumours from SCID xenografted mice was extracted using RNeasy Plus Mini Kit (Qiagen) according to the manufacturer's protocol. cDNA was produced using High-Capacity cDNA Reverse Transcription Kit (Applied Biosystems) using 500 ng of total RNA. qRT-PCRwas performed with Taqman miRNA assays and Taqman probes FAM-MGB for miR-205, miR-221, VEGF, *LAMC1, E2F1, p53, E-cadherin, Snail1* and *Slug* (*Snail2*) (Applied Biosystems). RNU6B was used as a reference gene. The reactions were processed using a Light Cycler 480 II Real-time PCR machine (Roche) using TaqMan Gene Expression Master Mix (Applied Biosystems) under the following cycling steps: 2 min at 50 °C for UNG activation; 10 min at 95 °C; 40 cycles at 95 °C for 15 s; 60 °C for 60 s. At least three independent repeats for each experiment were carried out. Gene expression was determined as a difference in fold after normalizing to the housekeeping gene RNU6B.

Development of orthotopic triple-negative breast cancer mice model

Tumours in the mammary fat pad were induced in female SCID hairless congenic mice (SHC Mouse CB17.Cg-Prkdc^{scid}Hr^{hr}/IcrCrl from Charles River Laboratories International, 6 weeks, $n = 5$) by injection of 5×10^6 MDA-MB-231 cells stably expressing firefly luciferase, suspended in 50 μl of HBBS (Lonza) solution. For determination of tumour growth, individual tumours were measured using a calliper and tumour volume was calculated by: tumour volume (mm^3) = width × (length^2)/2. Treatments began when tumour volume reached about 100 mm^3. All experimental protocols were approved by the MIT

Animal Care and Use Committee and were in compliance with NIH guidelines for animal use.

RNA-triple-helix hydrogel scaffold synthesis and *in vivo* implantation

Tagged hydrogel scaffolds were developed as previously described[50]. Briefly, equal parts of dendrimer amine of 12.5% solid content and dextran aldehyde 5% solid content with 0.25% fluorescently labelled dextran were mixed to form 6 mm pre-cured disks. For doped scaffolds, RNA nanoparticles (1 μM of RNA oligonucleotides doped in 5% PAMAM dendrimer generation 5 with 100% amines) or the free drugs: doxorubicin (DOX, from LC Laboratories), paclitaxel (PTX, from LC Laboratories) and the monoclonal antibody bevacizumab (Avastin, from Roche) were added to the dendrimer solution before hydrogel formation. All solutions were filtered through a 0.22 μm filter before hydrogel formation for *in vivo* implantation. Pre-cured disks of fluorescently labelled scaffold with or without RNA nanoparticles were formed and implanted subcutaneously on top of the mammary tumour in mice.

Dextran aldehyde tagging reaction

Dextran aldehyde (Mr 10,000 Da, 50% oxidation; 10 mg) was tagged byreaction with 2 mg ofAlexa Fluor 405 Cadaverine (Invitrogen) in 20 ml of 50 mM carbonate buffer (pH 8.5) for 1 h at room temperature. Then, the reaction crude was cooled down in an ice-water bath and imine bonds were reduced with 20 ml of 30 mM sodium cyanoborohydrate in PBS for 4 h. Then, tagged dextran aldehyde was dialysed four times through a 3,000 Da MWCO Centrifugal Filter (Millipore) for 20 min each time at room temperature and 4,000 RCFs. The purified product was lyophilized.

RNA-triple-helix hydrogel scaffold fluorescence images

Pre-cured fluorescently labelled scaffolds alone (control) or doped with triple-helix nanoparticles with or without target pre-incubation were snap-frozen in liquid nitrogen and kept at −80 °C for 24 h. Then, 12 μm-thick cryosections (Cryostat Leica CM1850) were analysed by fluorescence microscopy (NIS-Elements Nikon). Controls for this experiment included empty scaffold (without nanoparticles) and scaffold with non-hybridized triple helices (quenched fluorescence from the oligonucleotides).

RNA-triple-helix release from hydrogel scaffold *in vitro*

Pre-cured disks of fluorescently labelled hydrogel scaffold alone or doped with triple-helix nanoparticles with or without target pre-hybridization were incubated in phosphate buffer saline (PBS) at 37 °C. At different time points, samples were collected from the PBS and fluorescence of released products was quantified (Varioskan Flash Multimode Reader, Thermo Scientific). Data were plotted as the percentage of total hybridized oligo or dextran aldehyde released for each time point. Controls for this experiment included empty scaffold (without nanoparticles) and scaffold with non-hybridized triple helices (quenched fluorescence from the oligonucleotides).

Analysis of tumour growth and RNA-triple-helix hydrogel scaffold degradation

Non-invasive longitudinal monitoring of tumour progression was followed by scanning mice with the IVIS Spectrum-bioluminescent and fluorescent imaging system (Xenogen XPM-2 Corporation) from mice bearing mammary tumours from MDA-MB-231 cells (n = 5 animals per treated group). 15 min before imaging, mice were intraperitoneally injected with 150 μl of D-luciferin (30 mg ml^{-1}, Perkin Elmer) in DPBS (Lonza). Whole-animal imaging was performed at the indicated time points—0, 2, 6, 24, 48, 72 h and days 5, 7, 9 and 13. Assessment of *in vivo* toxicity via mice body weight evaluation was performed on all the animal groups during 32 days after tumour induction and hydrogel exposure. Histological sections of the tumours ($n = 5$) were stained with haematoxylin and eosin and for immunohistochemical analysis the tumours ($n = 5$) were stained with the antibody anti-Ki67 (Abcam ab15580, dilution 1:200).

Statistics

Differences between groups were examined using a two-tailed Student's *t*-test, two-way analysis of variance (ANOVA) or Log-Rank Mantel–Cox test through the SPSS statistical package (version 23, SPSS). All error bars used in this report are mean ± s.d. of at least three independent experiments. Statistically significant *P* values are indicated in figures and/or legends as ***, $P < 0.005$; **, $P < 0.01$; *, $P < 0.05$. All *in vivo* experiments used five per treatment group. No randomization or blind events were used in animal studies.

Supplementary Material

Refer to Web version on PubMed Central for supplementary material.

Acknowledgements

J.C. acknowledges a Marie Curie International Outgoing Fellowship and Funding (FP7-PEOPLE-2013-IOF, Project 626386). We thank D. Fulop for helpful and fruitful discussions. We thank the Swanson Biotechnology Center at the Koch Institute for Integrative Cancer Research at Massachusetts Institute of Technology (MIT) for assistance with animal experiments and facilities, especially the microscopy, flow cytometry, and histology cores. We also acknowledge that all qPCR experiments done in the KI Genomics Core/MIT BioMicro Center are funded by the NIH and supported in partby the Koch Institute Support Grant P30-CA14051 from the National Cancer Institute and by the National Institute of Environmental Health Sciences of the NIH under award P30-ES002109. We thank D. S. Yun for cryo-TEM assistance at the Peterson Nanotechnology Materials Core Facility. We thank the Department of Comparative Medicine at MIT, especially J. Haupt. We thank G. Paradis for FACS assistance with Cancer Center Support (FACS core) Grant P30-CA14051 from the National Cancer Institute. We thank P. Boisvert and Y. Zhang for technical assistance in SEM at the MIT Center for Materials Science and Engineering (CMSE). These SEM studies made use of the MRSEC Shared Experimental Facilities at MIT, supported by the National Science Foundation under award number DMR-1419807.

References

1. Kasinski AL & Slack FJ MicroRNAs en route to the clinic: Progress in validating and targeting microRNAs for cancer therapy. Nature Rev. Cancer 11, 849–864 (2011). [PubMed: 22113163]
2. Li Z & Rana TM Therapeutic targeting of microRNAs: Current status and future challenges. Nature Rev. Drug Discov 13, 622–638 (2014). [PubMed: 25011539]
3. Yin H et al. Non-viral vectors for gene-based therapy. Nature Rev. Genet 15, 541–555 (2014). [PubMed: 25022906]

4. Conde J, Edelman ER & Artzi N Target-responsive DNA/RNA nanomaterials for microRNA sensing and inhibition: The jack-of-all-trades in cancer nanotheranostics? Adv. Drug Deliv. Rev 81, 169–183 (2015). [PubMed: 25220355]
5. Chen YC, Gao DY & Huang L In vivo delivery of miRNAs for cancer therapy: Challenges and strategies. Adv. Drug Deliv. Rev 81, 128–141 (2015). [PubMed: 24859533]
6. Yin PT, Shah BP & Lee KB Combined magnetic nanoparticle-based microRNA and hyperthermia therapy to enhance apoptosis in brain cancer cells. Small 10, 4106–4112 (2014). [PubMed: 24947843]
7. Hao LL, Patel PC, Alhasan AH, Giljohann DA & Mirkin CA Nucleic acid-gold nanoparticle conjugates as mimics of microRNA. Small 7, 3158–3162 (2011). [PubMed: 21922667]
8. Endo-Takahashi Y et al. Systemic delivery of miR-126 by miRNA-loaded bubble liposomes for the treatment of hindlimb ischemia. Sci. Rep 4, 3883 (2014). [PubMed: 24457599]
9. Chen YC, Zhu XD, Zhang XJ, Liu B & Huang L Nanoparticles modified with tumor-targeting scFv deliver siRNA and miRNA for cancer therapy. Mol. Ther 18, 1650–1656 (2010). [PubMed: 20606648]
10. Anand S et al. MicroRNA-132-mediated loss of p120RasGAP activates the endothelium to facilitate pathological angiogenesis. Nature Med. 16, 909–914 (2010). [PubMed: 20676106]
11. Wu Y et al. MicroRNA delivery by cationic lipoplexes for lung cancer therapy. Mol. Pharm 8, 1381–1389 (2011). [PubMed: 21648427]
12. Mittal A, Chitkara D, Behrman SW & Mahato RI Efficacy of gemcitabine conjugated and miRNA-205 complexed micelles for treatment of advanced pancreatic cancer. Biomaterials 35,7077–7087 (2014). [PubMed: 24836307]
13. Cheng CJ et al. MicroRNA silencing for cancer therapy targeted to the tumour microenvironment. Nature 518, 107–110 (2015). [PubMed: 25409146]
14. Shu D et al. Systemic delivery of Anti-miRNA for suppression of triple negative breast cancer utilizing RNA nanotechnology. ACS Nano 9, 9731–9740 (2015). [PubMed: 26387848]
15. McKiernan PJ, Cunningham O, Greene CM & Cryan SA Targeting miRNA-based medicines to cystic fibrosis airway epithelial cells using nanotechnology. Int. J. Nanomed 8, 3907–3915 (2013).
16. Cheng CJ & Saltzman WM Polymer nanoparticle-mediated delivery of microRNA inhibition and alternative splicing. Mol. Pharm 9, 1481–1488 (2012). [PubMed: 22482958]
17. Guo P X. The emerging field of RNA nanotechnology. Nature Nanotech. 5, 833–842 (2010).
18. Lee JB, Hong J, Bonner DK, Poon Z & Hammond P T. Self-assembled RNA interference microsponges for efficient siRNA delivery. Nature Mater 11, 316–322 (2012). [PubMed: 22367004]
19. Mok H, Lee SH, Park JW & Park TG Multimeric small interfering ribonucleic acid for highly efficient sequence-specific gene silencing. Nature Mater. 9, 272–278 (2010). [PubMed: 20098433]
20. Lee H et al. Molecularly self-assembled nucleic acid nanoparticles for targeted in vivo siRNA delivery. Nature Nanotech. 7, 389–393 (2012).
21. Haque F et al. Ultrastable synergistic tetravalent RNA nanoparticles for targeting to cancers. Nano Today 7, 245–257 (2012). [PubMed: 23024702]
22. Shu D, Shu Y, Haque F, Abdelmawla S & Guo P X. Thermodynamically stable RNA three-way junction for constructing multifunctional nanoparticles for delivery of therapeutics. Nature Nanotech. 6, 658–667 (2011).
23. Jendis J, Strack B &Moelling K Inhibition of replication of drug-resistant HIV type 1 isolates by polypurine tract-specific oligodeoxynucleotide TFO A. AIDS Res. Hum. Retroviruses 14, 999–1005 (1998). [PubMed: 9686646]
24. Moelling K, Abels S, Jendis J, Matskevich A & Heinrich J Silencing of HIV by hairpin-loop-structured DNA oligonucleotide. FEBS Lett. 580, 3545–3550 (2006). [PubMed: 16737697]
25. Yoon K, Hobbs CA, Walter AE & Turner DH Effect of a 5′-phosphate on the stability of triple helix. Nucleic Acids Res. 21, 601–606 (1993). [PubMed: 8441671]
26. Chan PP & Glazer PM Triplex DNA: Fundamentals, advances, and potential applications for gene therapy. J. Mol. Med 75,267–282 (1997). [PubMed: 9151213]

27. Holland JA & Hoffman DW Structural features and stability of an RNA triple helix in solution. Nucleic Acids Res. 24, 2841–2848 (1996). [PubMed: 8759020]
28. Duca M, Vekhoff P, Oussedik K, Halby L & Arimondo P B. The triple helix: 50 years later, the outcome. Nucleic Acids Res. 36, 5123–5138 (2008). [PubMed: 18676453]
29. Foulkes WD, Smith IE & Reis JS Triple-negative breast cancer. N. Engl. J. Med 363, 1938–1948 (2010). [PubMed: 21067385]
30. Nassirpour R, Mehta PP, Baxi SM & Yin MJ miR-221 promotes tumorigenesis in human triple negative breast cancer cells. PLoS ONE 8, e62170 (2013). [PubMed: 23637992]
31. Piovan C et al. Oncosuppressive role ofp53-induced miR-205 in triple negative breast cancer. Mol. Oncol 6, 458–472 (2012). [PubMed: 22578566]
32. Conde J, Oliva N & Artzi N Implantable hydrogel embedded dark-gold nanoswitch as a theranostic probe to sense and overcome cancer multidrug resistance. Proc. Natl Acad. Sci. USA 112, E1278–E1287 (2015). [PubMed: 25733851]
33. Oliva N et al. Regulation of dendrimer/dextran material performance by altered tissue microenvironment in inflammation and neoplasia. Sci. Transl. Med 7, 272ra211 (2015).
34. Schroeder A, Levins CG, Cortez C, Langer R & Anderson DG Lipid-based nanotherapeutics for siRNA delivery. J. Int. Med 267, 9–21 (2010).
35. Francois JC et al. Sequence-specific recognition and cleavage of duplex DNA via triple-helix formation by oligonucleotides covalently linked to a phenanthroline copper chelate. Proc. Natl Acad. Sci. USA 86, 9702–9706 (1989). [PubMed: 2557624]
36. Chiou CC, Chen SW, Luo JD & Chien YT Monitoring triplex DNA formation with fluorescence resonance energy transfer between a fluorophore-labeled probe and intercalating dyes. Anal. Biochem 416, 1–7 (2011). [PubMed: 21609711]
37. Wan CH, Cui M, Song FR, Liu ZQ & Liu SY Evaluation of effects of bivalent cations on the formation of purine-rich triple-helix DNA by ESI-FT-MS. J. Am. Soc. Mass Spectrom 20, 1281–1286 (2009). [PubMed: 19297188]
38. Carlson RD, Olins AL & Olins DE Urea denaturation of chromatin periodic structure. Biochemistry 14, 3122–3125 (1975). [PubMed: 1148192]
39. Ha M & Kim V N. Regulation of microRNA biogenesis. Nature Rev. Mol. Cell Biol 15, 509–524 (2014). [PubMed: 25027649]
40. Conner SD & Schmid SL Regulated portals of entry into the cell. Nature 422, 37–44 (2003). [PubMed: 12621426]
41. Conde J et al. 15 years on siRNA delivery: Beyond the State-of-the-Art on inorganic nanoparticles for RNAi Therapeutics. Nano Today 10.1016/jmantod.2015.06.008 (in the press).
42. Kitchens KM, Kolhatkar IB, Swaan PW & Ghandehari H Endocytosis inhibitors prevent poly(amidoamine) dendrimer internalization and permeability across Ceco-2 cells. Mol. Pharm 5, 364–369 (2008). [PubMed: 18173246]
43. Jones AT Macropinocytosis: Searching for an endocytic identity and role in the uptake of cell penetrating peptides. J. Cell Mol. Med 11, 670–684 (2007). [PubMed: 17760832]
44. Linares J et al. Endocytic mechanisms of graphene oxide nanosheets in osteoblasts, hepatocytes and macrophages. ACS Appi. Mater. Interfaces 6, 13697–13706 (2014).
45. Iversen TG, Skotland T & Sandvig K Endocytosis and intracellular transport of nanoparticles: Present knowledge and need for future studies. Nano Today 6, 176–185 (2011).
46. Segovia N et al. Hydrogel doped with nanoparticles for local sustained release of siRNA in breast cancer. Adv. Healthc. Mater 4, 271–280 (2015). [PubMed: 25113263]
47. Sledge GW et al. Past, present, and future challenges in breast cancer treatment. J. Clin. Oncol 32, 1979–1986 (2014). [PubMed: 24888802]
48. Sparano JA et al. Weekly paclitaxel in the adjuvant treatment ofbreast cancer. N. Engl. J. Med 358, 1663–1671 (2008). [PubMed: 18420499]
49. Miller K et al. Paclitaxel plus bevacizumab versus paclitaxel alone for metastatic breast cancer. N. Engl. J. Med 357,2666–2676 (2007). [PubMed: 18160686]
50. Oliva N et al. Natural tissue microenvironmental conditions modulate adhesive material performance. Langmuir 28, 15402–15409 (2012). [PubMed: 23046479]

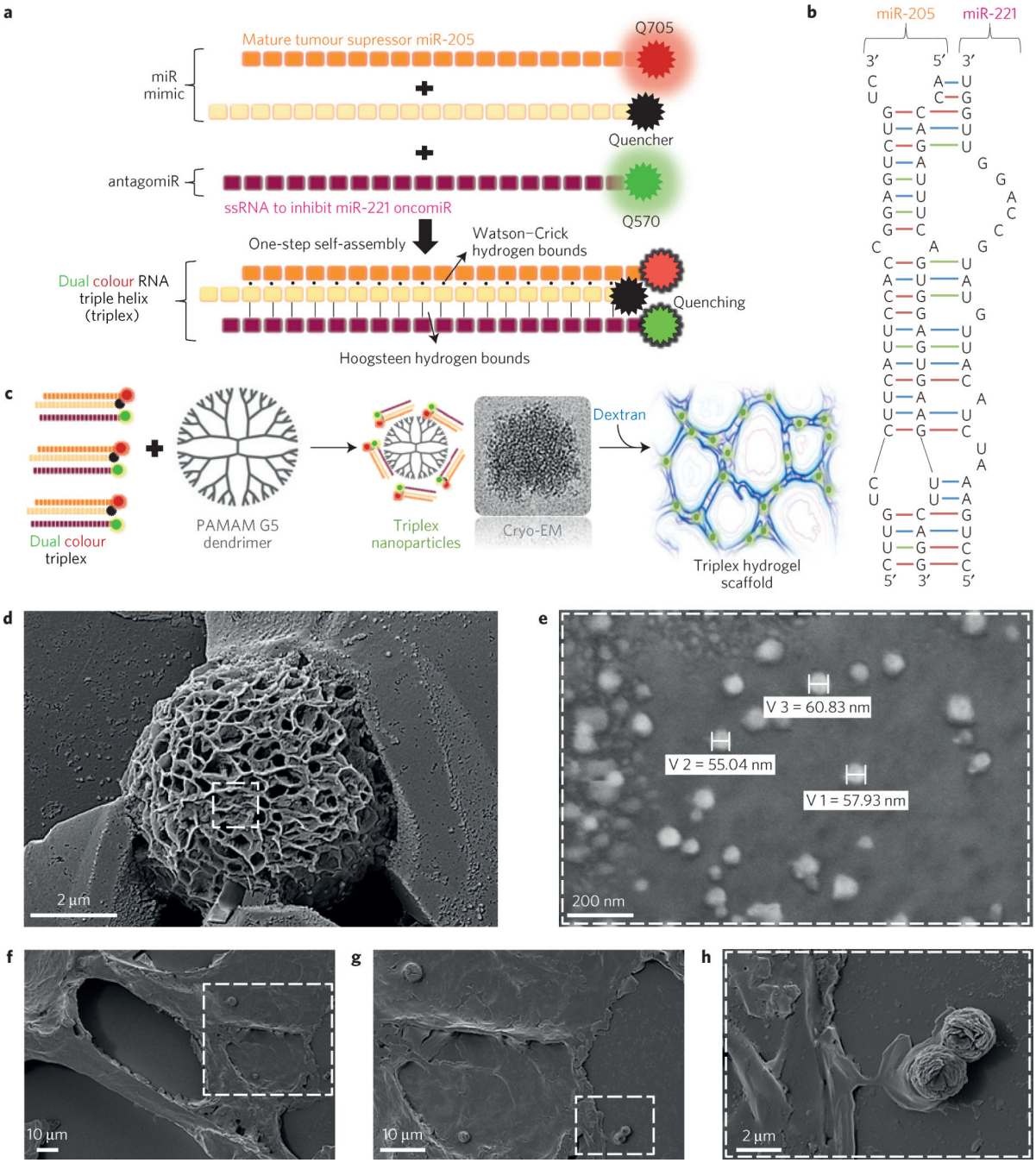

Figure 1 |. Self-assembled RNA-triple-helix hydrogel nanoconjugates and scaffold for microRNAdelivery.

a, Schematic showing the self-assembly process of three RNA strands to form a dual-colour RNA triple helix. The RNA triplex nanoparticles consist of stable two-pair FRET donor/quencher RNA oligonucleotides used for *in vivo* miRNA inhibition (miR-221 antagomiR) strategy and miRNA replacement therapy (miR-205 mimic). **b**, Secondary structure of an RNA triple helix bearing both miR-205 mimic and miR-221 antagomiR (structure produced/adapted using M-fold software). **c**, Formation of the RNA-triple-helix hydrogel scaffolds by conjugation of the RNA-triple-helix structure to PAMAM G5 (Cryo-EM image showing the

branched sponge-like nanoscopic structure) followed by reaction with oxidized dextran to form the adhesive hydrogel. **d**,**e**, High-resolution SEM image of RNA microstructures (3.4 ± 1.1 μm) (**d**) composed of small RNA-triple-helix-dendrimer nanoparticles (56.6 ± 3.9 nm) (**e**). **f-h**, High-resolution SEM images of RNA macrostructures embedded in the dextran-dendrimer hydrogel scaffolds.

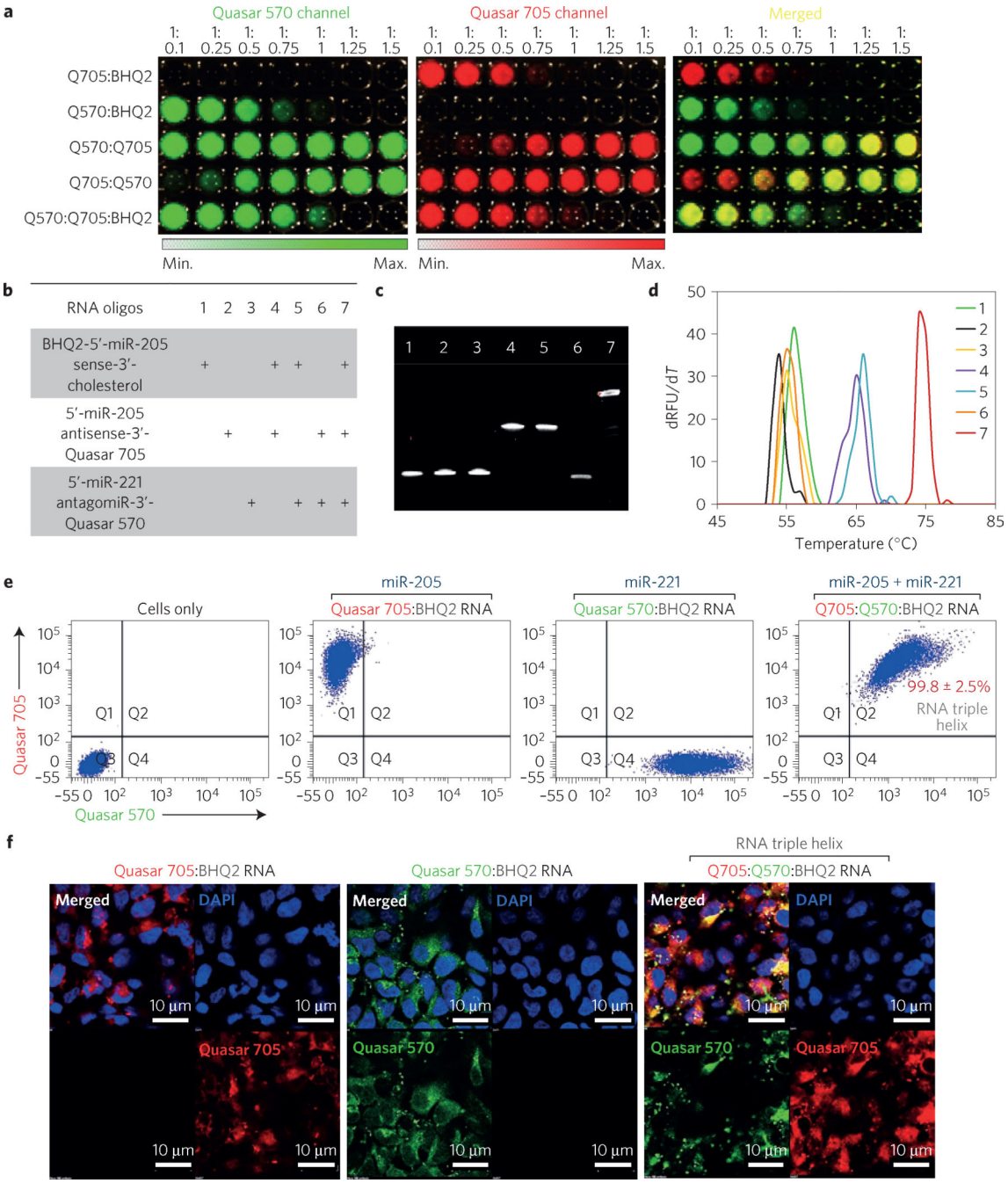

Figure 2 |. RNA-triple-helix assembly/stability assays and *in vitro* cellular uptake of RNA-dendrimer nanoparticles into cancer cells.

a, Evaluation of the fluorescence intensity of the different RNA oligonucleotides at several molar ratios at room temperature using a live imaging system, to compare quenching efficiencies induced by the proximity of the chromophores with the quencher BHQ2. **b**, RNA combinations are depicted in the table by '+' signs, indicating the presence of a specific RNA strand. **c**, Gel electrophoresis showing self-assembly of the RNA triple helix (lane 7) and all other oligo combinations depicted in **b**. **d**, First derivative of the melting temperature (T_m) curves for the assembly of the different oligo combinations described in **b**.

e, Flow cytometry revealed the specific uptake of fluorescent RNA-dendrimer nanoparticles into MDA-MB-231 cells. Negative and positive controls were cells only and cells treated with the RNA double helices (Q705:BHQ2 and Q570:BHQ2), respectively. Q1, the cell population containing the dye Quasar 705; Q4, containing the dye Quasar 570; Q2 containing both dyes and Q3 with no fluorescence signal. **f**, Confocal images showing strong uptake of the RNA-dendrimer complexes, as demonstrated by the outstanding co-localization of the dual-colour RNA triple helix (Q705:Q570:BHQ2). Nuclei (in blue) were stained with DAPI. Scale bars, 10 μm. All experiments were done in triplicate and errors reported as standard deviation (s.d.).

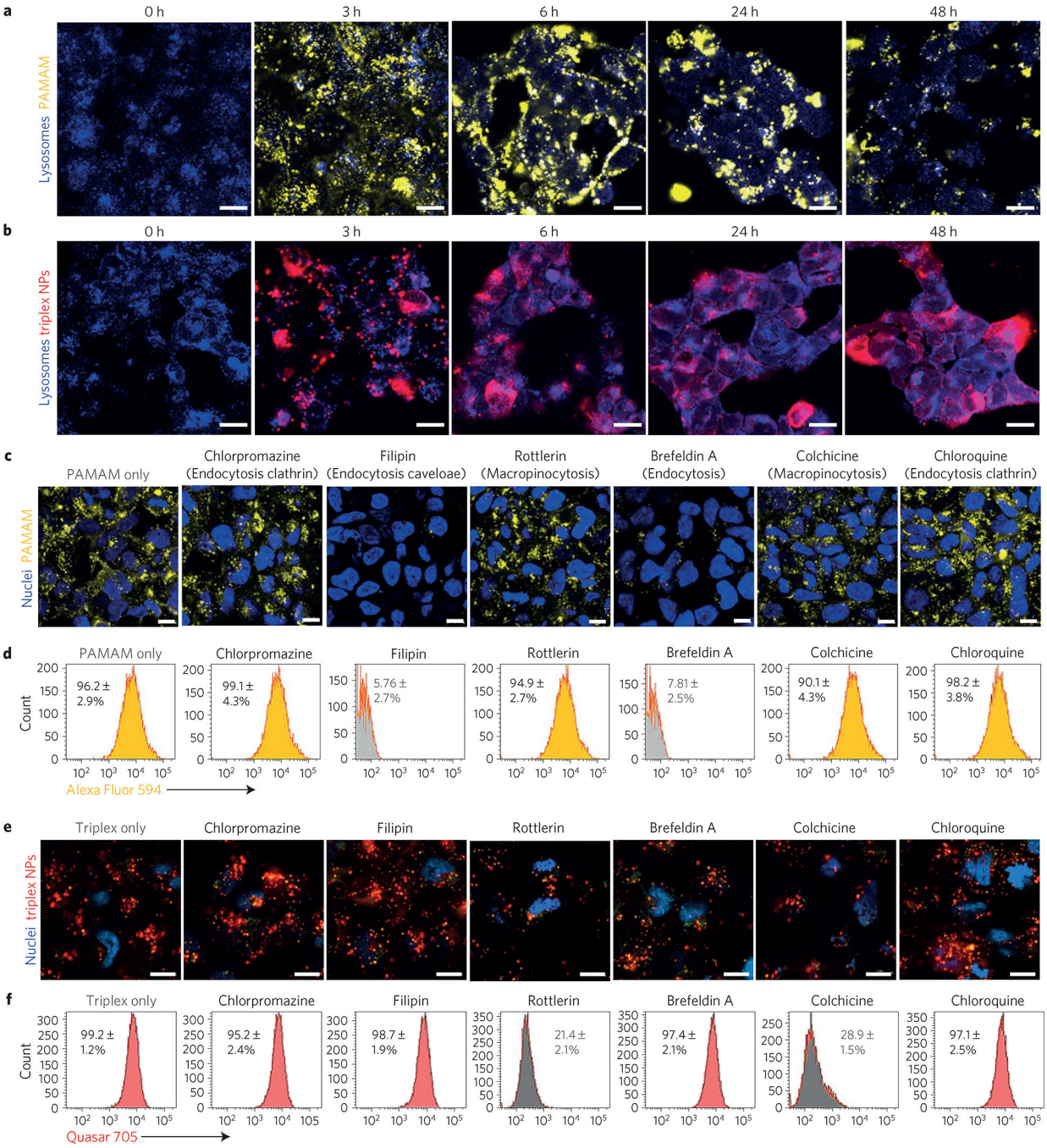

Figure 3 |. Cellular trafficking and uptake mechanism of naked dendrimer and RNA-triple-helix-dendrimer conjugates.

a,**b**, Lysosomal co-locallzatlon in cells incubated for 0, 3, 6, 24 and 48 h with naked PAMAM G5 dendrimer (**a**) and RNA-triple-helix-dendrimer nanoparticles, NPs (**b**). Lysosomes (in blue) were stained with LysoTracker Blue DND-22. c,d, Confocal microscopy images (**c**) and quantification by analytical flow cytometry (**d**) of the internalization and sub-cellular localization of naked PAMAM G5 dendrimer in the presence of several small-molecule inhibitors. **e**,**f**, Confocal microscopy images (**e**) and quantification

by analytical flow cytometry (**f**) of the internalization and sub-cellular localization of triplex-dendrimer nanoparticles in the presence of several small-molecule inhibitors. Scale bars, 5 μm. All experiments were done in triplicate and errors are reported as standard deviation (s.d.).

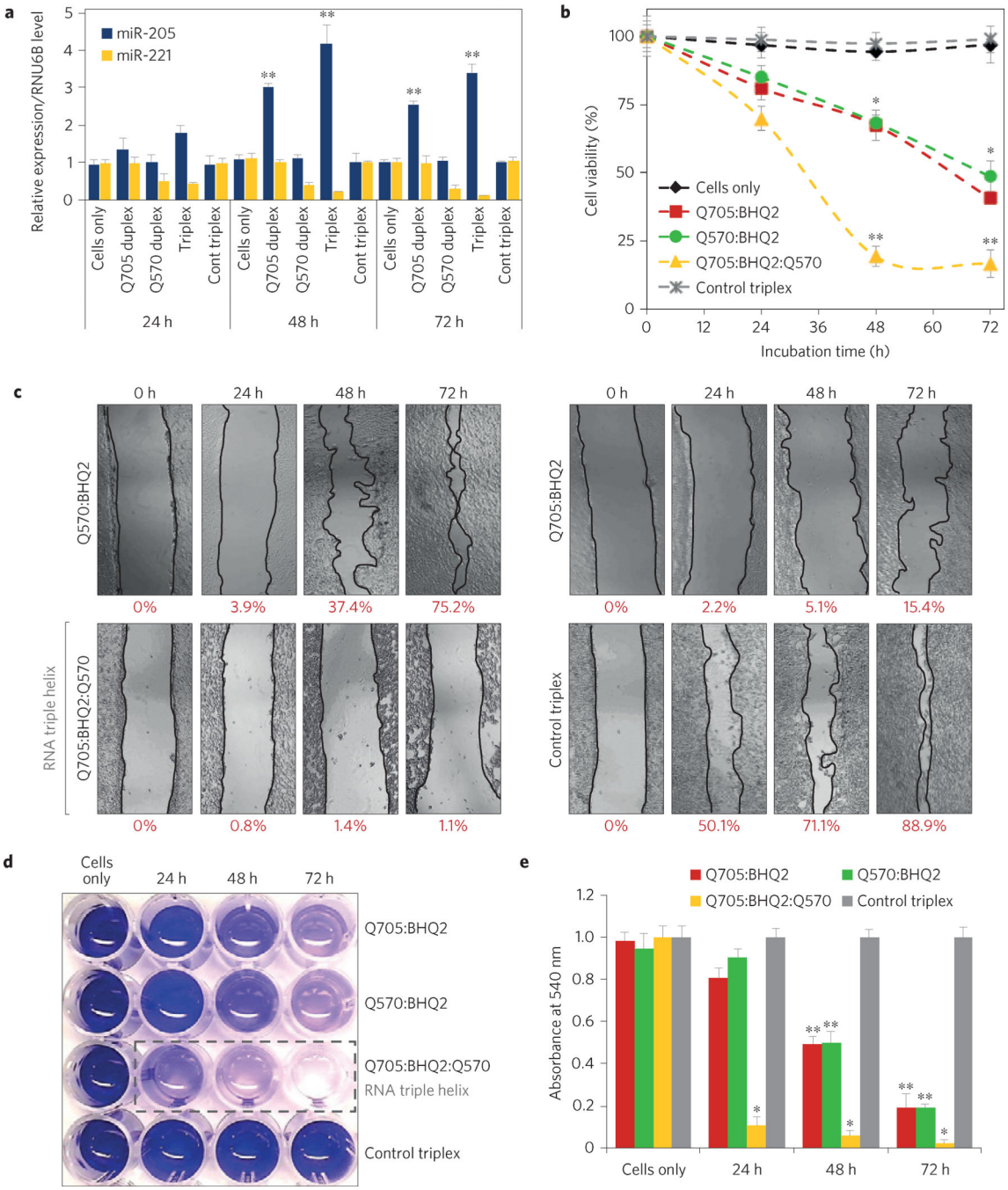

Figure 4 |. Proliferation, migration and survival of cancer cells as a function of RNA-triple-helix nanoparticles treatment.

a, miR-205 and miR-221 expression in breast cancer cells at 24, 48 and 72 h of incubation ($n = 3$, statistical analysis performed with a two-tailed Student's *t*-test, **, $P < 0.01$). miRNA levels were normalized to the *RNU6B* reference gene. **b**, Cell viability via an MTT assay for 24, 48 and 72 h ($n = 3$, statistical analysis performed with a two-tailed Student's *t*-test, **, $P < 0.01$; *, $P < 0.05$). **c**, RNA-triple-helix nanoparticles restrict MDA-MB-231 cell migration. **d**,**e**, The number of colonies in the cells transfected with the RNA triple helix was

compared with the control triplex at 24, 48 and 72 h of incubation (**d**). Graph (**e**) depicts the absorbance ofthe crystal-violet-stained colonies (dissolved in methanol) at 540 nm ($n = 3$, statistical analysis performed with a two-tailed Student's *t*-test, **, $P < 0.01$; *, $P < 0.05$). All experiments were done in triplicate and error bars plotted as standard deviation (s.d.).

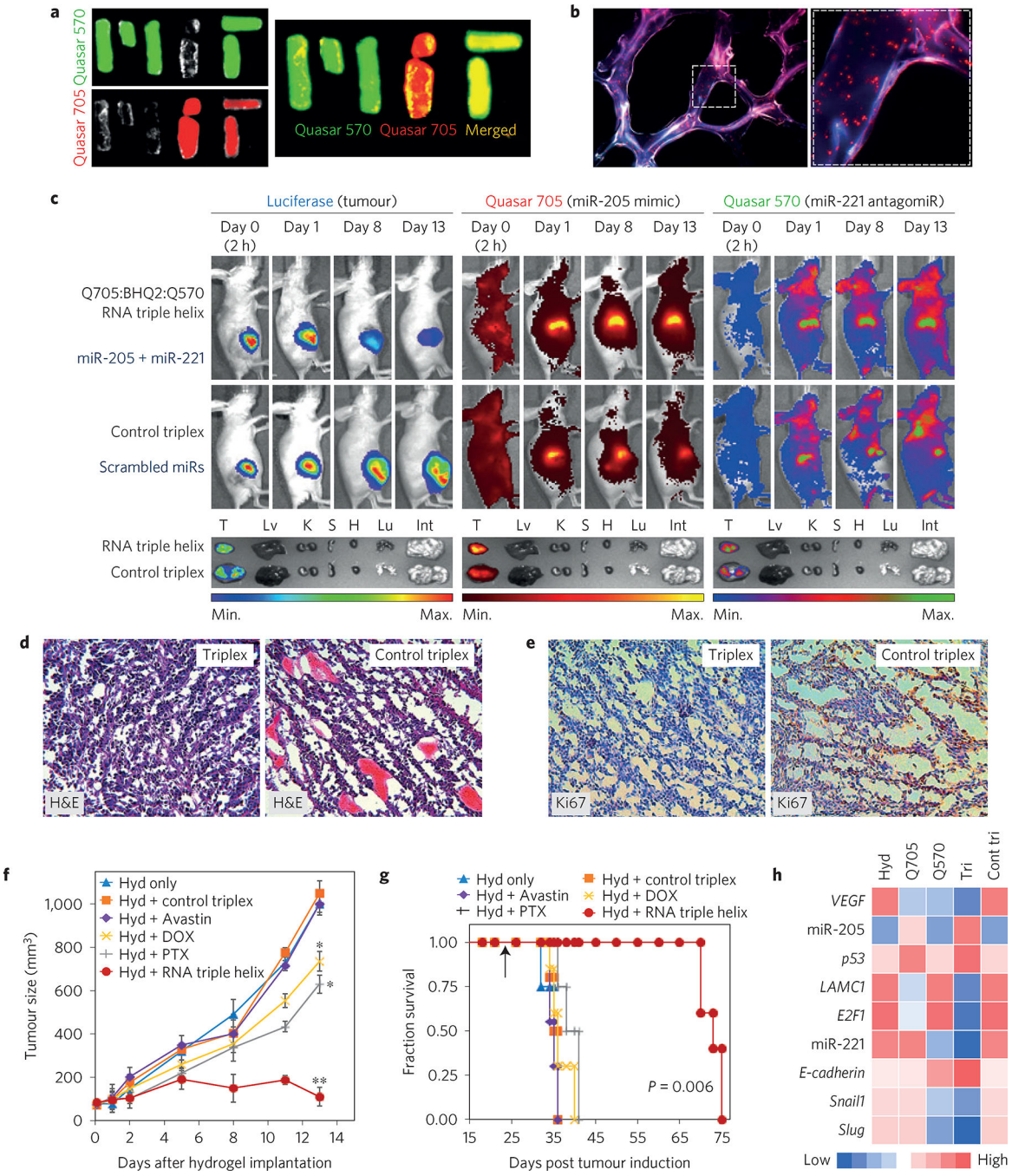

Figure 5 |. *In vivo* miRNA modulation and tumour therapy via RNA-triple-helix hydrogel scaffolds.

a, Dual-colour hydrogel scaffolds made of RNA-triple-helix nanoconjugates pre-lncubated with complementary mIR targets. **b**, Cryosectlon of dendrlmer-dextran adhesive hydrogel (12 μm thickness) depicting adhesive morphology (dextran aldehyde was tagged with Alexa Fluor 405). Red spots represent the triple-helix nanoparticles containing Q705 (red) and Q570 (green) oligonucleotides. **c**, Live imaging of female SCID hairless congenic mice with triple-negative breast tumour xenograft implanted with hydrogels embedded with RNA-

triple-helix nanoparticles and with a control triplex (scrambled miRs), (n = 5 per group). *Ex vivo* images of breast tumours and whole body organs (T, tumour; Lv, liver; K, kidneys; S, spleen; H, heart; Lu, lung; Int, intestines) are also presented. **d**, Haematoxylin and eosin (H&E) stains of tumours from treated groups with hydrogels embedded with RNA-triple-helix nanoparticles and with a control triplex (scrambled miRs). **e**, Immunohistochemical evaluation of tumours treated with hydrogels embedded with RNA-triple-helix nanoparticles and with a control triplex for Ki67 to evaluate tumour cell proliferation. **f**, Tumour size following treatment (n = 5, statistical analysis performed with a two-way ANOVA, **, P< 0.01; *, P< 0.05). Individual tumours were measured using a Vernier calliper and tumourvolume was calculated by: tumourvolume (mm^3) = width × ($length^2$)/2. **g**, Kaplan-Meier curves for mice treated with hydrogel scaffolds loaded with triple-helix and control triple-helix nanoparticles, as well as for the drugs (DOX, PTX and Avastin). Statistical analysis (n = 5) was performed with a Log-Rank Mantel-Cox test (P = 0.006). Survival cutoff criteria included tumour ulceration or compassionate euthanasia, aggregate tumour burden >1 cm in diameter, or if tumour impedes eating, urination, defecation or ambulation. Arrow represents the day of hydrogel implantation (day 22 post tumour induction). **h**, Heat-map summary of gene expression profiling of the miRs and their related genes that play key roles in cancer progression and migration.